Experiments on a turbulent plume: Shape analyses

Shogo Kitamura[1] and Ikuro Sumita[1]

Received 11 April 2010; revised 18 December 2010; accepted 12 January 2011; published 30 March 2011.

[1] We report the results of laboratory experiments on a turbulent plume, a simplified model of a positively buoyant volcanic plume with a small content of fine ash to study how the shape of the plume changes as a function of time. To model such plumes, we continuously inject a dense fluid downward at a constant exit velocity and study how the plume shape changes with time as vortices develop from flow instability and entrainment. Here a series of experiments are conducted with exit velocity and the density difference as the changeable parameters, and the jet-plume transition is realized in the laboratory. Initially the plume has a "finger-like" shape which becomes unstable and forms a "plume head" and later transforms into a "cone-like" self-similar shape. We also find that when the buoyancy becomes sufficiently large compared to inertia, there is a temporary deviation from the cone-like shape to form a "headed cone." We devise new methods to quantitatively characterize these changes of shape and define four regimes as a function of time. We find that the onset times of the flow instability and the regimes have negative power law dependence on the initial *Re* (or the exit velocity), and that buoyancy causes the regime transitions to become earlier. Our experiments suggest that monitoring the change of the shape of the rising volcanic plumes and analyzing the regime onset times, can be used as a measure to constrain their buoyancy.

Citation: Kitamura, S., and I. Sumita (2011), Experiments on a turbulent plume: Shape analyses, *J. Geophys. Res.*, *116*, B03208, doi:10.1029/2010JB007633.

1. Introduction

[2] Turbulent plumes which are characterized by a large Reynolds number ($Re \gg 1$) and buoyancy are ubiquitous in nature, an example of which is a volcanic plume. As the turbulent plume rises, it entrains the ambient fluid and grows in size. When sufficiently developed, it transforms into a characteristic self-similar cone-like shape. Many laboratory experiments have been conducted to study turbulent plumes [e.g., *List*, 1982; *Papanicolaou and List*, 1988; *Ai et al.*, 2006; *Kaye and Hunt*, 2009]. These studies have primarily focused on the developed stage in which the plume becomes cone-like as a result of self-similar flow being established. Such self-similarity is a consequence of entrainment constant, which is the ratio of the horizontal inflowing velocity to the axial velocity, becoming time-independent. An analytical model [*Morton et al.*, 1956] has been constructed based on this assumption, which has been used in models of eruption columns [e.g., *Woods*, 1988].

[3] In turbulent plumes a certain time or distance is needed after exiting from the orifice before transforming into a cone-like shape, and many of the volcanic plumes which we observe are also in this transitionary stage. In addition, when the plume has a sufficient buoyancy, the driving force of the front of the plume changes with time. The plume is initially driven by inertia arising from the overpressure at its source (jet-like) which is gradually lost and is overtaken by the buoyancy (plume-like). In volcanic plumes, the height ranges of these two stages have been termed as "gas thrust" and "convective" regions, respectively [e.g., *Sparks*, 1986; *Woods*, 1988]. However it is only quite recently that detailed investigations on the transition have been made. *Patrick* [2007a] analyzed video images in Strombolian ash plumes and studied how the shape evolves with time, and found that the shape and height-time relation of the plumes can be classified according to the exit velocity.

[4] There have been few laboratory experiments and their analyses focusing on such transitionary stage. *Carazzo et al.* [2006] showed that the variation of the values of the entrainment constants obtained in previous experiments on jets and plumes can be interpreted as a consequence of such evolution. Detailed study on the evolution of flow pattern and entrainment constant for jets and positively buoyant plumes have been made for example by *Ai et al.* [2006]. Here, positive buoyancy corresponds to the case in which the buoyancy acts in the direction in which the fluid is being injected. There have also been several experiments which model the negatively and reversing buoyancy cases [e.g., *Woods and Caulfield*, 1992; *Kaminski et al.*, 2005; *Papanicolaou et al.*, 2008]. In a recent study focusing on the near field of a jet, *Solovitz and Mastin* [2009] showed that the entrainment constant is indeed small in the near field of the orifice compared to the far field in which the flow becomes fully developed. These experiments

[1]Graduate School of Natural Science and Technology, Kanazawa University, Kanazawa, Japan.

0148-0227/11/2010JB007633

have primarily focused on how the flow field of turbulent plumes transform from the near field (developing stage) to the far field (fully developed stage) as a function of initial *Re* (exit velocity) and buoyancy. However there have been no experimental studies focusing on the temporal change of the shape of the turbulent plume and how they differ with these parameters. The shape of the volcanic plume can be analyzed from video recordings. If we know the relation between the shape of the turbulent plume and these parameters, it may be used to constrain them, because *Re* and buoyancy are functions of initial velocity and source temperature.

[5] In this paper, we report the results of a series of experiments in which the initial *Re* and buoyancy are varied by changing the exit velocity and density difference, respectively. We focus on devising new methods to characterize the temporal change of the plume shape, and then use them to clarify how the parameters control these changes. Our experiments model the positively buoyant volcanic plumes with a small content of fine ash, such as the Strombolian volcanic plumes, as we show in section 2. Our study focusing on the case without solid particles would be the first step to understand the more complicated cases in which the solid particles separate from the flow as well as the negatively or reversing buoyancy cases. We note that the exit velocity in our experiments is constant, whereas in volcanic eruptions it will change with time, which has been simulated in some laboratory experiments [*Kieffer and Sturtevant*, 1984; *Clarke et al.*, 2009]. Also, there is no density stratification of the ambient fluid in our experiments, which can become important in large-scale explosive eruptions [e.g.,*Carazzo et al.*, 2008]. We consider that experiments with a constant exit velocity in the ambient fluid with no stratification are needed before studying more complicated cases in which time dependency and density stratification become important.

[6] Video images of volcanic eruptions using a wide range of electromagnetic wavelengths are increasingly being recorded in the recent years [e.g., *Formenti et al.*, 2003; *Patrick*, 2007a; *Patrick et al.*, 2007; *Yamamoto et al.*, 2008; *Sahatapy-Engel and Harris*, 2009; *Mori and Burton*, 2009; *Yokoo*, 2009]. In addition, more realistic numerical simulations of volcanic plumes have become feasible [e.g., *Suzuki et al.*, 2005; *Ogden et al.*, 2008a, 2008b; *Suzuki and Koyaguchi*, 2009, 2010]. Our experiments are intended to provide the bases for interpreting the shape changes observed in such videos, and to compliment the numerical studies.

2. Conditions for a Positively Buoyant Plume With a Homogeneous Particle Distribution

[7] Here we consider when the actual volcanic plumes become positively buoyant and the volcanic ash are homogeneously distributed, a situation corresponding to our experiments.

[8] First we consider when the volcanic plumes become positively buoyant. For a pressure-balanced (1 atm) volcanic plume, density and volume are functions of the temperature and the mass fractions of the three components; the volcanic gas and solid particles in the ejected material, and the entrained air. When the volcanic plume entrains a colder ambient air, the plume cools while the entrained air is heated. As a consequence, the density and volume of the plume changes nonlinearly with entrainment whose expression is derived in Appendix A. The initial condition of the volcanic gas can be specified by its temperature T_0, and the mass fraction of the volcanic gas n_{g0} within the ejected material (equation (A1)). We can calculate how the density and volume of the volcanic plume change as the ambient air is entrained whose mass fraction is defined as ξ (equation (A2)).

[9] Figures 1a and 1b show examples of how the density and volume of the volcanic plume change with entrainment, for different values of n_{g0}. Similar calculations have been done for example by *Suzuki et al.* [2005] and *Patrick* [2007b]. Here we take the initial temperature as $T_0 = 1300$ K which is close to the value used by *Patrick* [2007b], and the ambient air temperature as $T_a = 300$ K (see Appendix A for the assumptions and details). In Figure 1, the density and volume of the volcanic plumes are nondimensionalized by the density of the ambient air and the total volume of the material ejected until the given mass fraction of air (ξ) is entrained, respectively.

[10] For $n_{g0} < 0.23$ (i.e., small initial gas content), volcanic plume is initially heavier than the ambient air (i.e., negatively buoyant) but its density decreases with entrainment such that it eventually becomes lighter than the ambient air. Such density decrease arises because the expansion of the entrained air by heating overwhelms the contraction of the hot volcanic gas by cooling. This is also apparent in Figure 1b in which the volume increase is larger when n_{g0} is smaller. As the entrainment proceeds, the plume density attains a minimum and thereafter increases. This is because with entrainment, the solid particles become diluted, and the density becomes primarily determined by the mixing of hot gas and the cold ambient air.

[11] On the other hand, for $n_{g0} \geq 0.23$, the volcanic plume is always lighter than the ambient air (i.e., positively buoyant). When the initial gas content becomes as large as $n_{g0} \geq 0.56$, the density of the plume increases monotonically with entrainment. For such case, expansion of the entrained air by heating is compensated by the contraction of volcanic gas by cooling, which is similar to our experiments in which we use incompressible fluids. Assuming that the heat capacities of the volcanic gas and ambient air are the same, the density change for $n_{g0} = 1.0$ is identical to the case in which a lighter liquid with a density difference of 7.70×10^2 kg m^{-3} is injected upward into water.

[12] In Figure 1c we classify three cases according to the style in which the density changes with entrainment as a function of initial temperature of the volcanic plume (T_0) and the initial mass fraction of the volcanic gas (n_{g0}). The region shown in grey corresponds to the case in which the density of the plume monotonically approach that of the ambient fluid, similar to our experimental situation.

[13] Mass fraction of volcanic gas in Strombolian volcanic plume is estimated to be high, typically $n_{g0} \sim 0.20$ [*Parfitt and Wilson*, 2008], $n_{g0} \geq 0.30$ [*Patrick*, 2007b], and as large as $n_{g0} \geq 0.7$ [*Chouet et al.*, 1974]. For most of these values of n_{g0}, with a typical initial gas temperature of $T_0 \sim$ 1300 K, the plume becomes lighter than the ambient air, as emphasized by *Patrick* [2007b]. This is in contrast to Plinian eruptions with a small gas content ($n_{g0} \leq 0.05$), which results in a plume that is initially heavier than air. For such case if the entrainment is insufficient, the plume collapses to form a pyroclastic flow [*Woods*, 1988; *Suzuki et al.*, 2005]. Vulcanian eruptions have gas fractions with a typical value of $n_{g0} \sim$

0.05 [*Parfitt and Wilson*, 2008], but if separation of gas occurs in the vent, it may exceed $n_{g0} \sim 0.1$ and become lighter than the ambient air. Indeed *Yamamoto et al.* [2008] measured the rise velocity of a vulcanian plume, and estimated its density, from which we can calculate the corresponding gas mass fraction as $n_{g0} \sim 0.4$.

[14] Next, we consider the condition under which the solid particles are homogeneously distributed within the plume. Particle distribution can become heterogeneous when the particle inertia is so large such that they do not follow the flow field, and when they are too heavy such that they settle. We evaluate each of these conditions below.

[15] The first condition can be evaluated using the Stokes number *St*, which is the ratio of the time scale in which the particle responds to the surrounding flow by viscous stress, and the characteristic time scale of flow (for example, the circulation time of the eddy),

$$St = \frac{\sigma r_p^2/\mu}{d/V} = \frac{\sigma r_p^2 V}{\mu d}, \tag{1}$$

where σ is the solid particle density, r_p is the particle radius, μ is the gas viscosity, d and V are the length and velocity scales, respectively, of the vortices. If $St \ll 1$ the particles closely follow the flow field, and vice versa at $St \gg 1$. Here we assume that the typical eddy size is of the order of the width of the vent diameter, as visualized by experiments by *Dimotakis et al.* [1983] for example. In the far field, larger vortices develop and therefore this can be considered as a lower limit estimate. We may evaluate V as a function of distance z from the vent exit using the plume model of *Morton et al.* [1956] as

$$V = \frac{5}{6\alpha}\left(\frac{9\alpha B_0}{10\pi}\right)^{\frac{1}{3}} z^{-\frac{1}{3}}, \tag{2}$$

where α is the entrainment constant (see section 5.4), $B_0 = \pi g(\Delta\rho/\rho_a)(d/2)^2 V_0$ is the initial specific buoyancy flux where g is the gravitational acceleration, $\Delta\rho = |\rho_{\text{plume}} - \rho_a|$ is the initial density difference between the plume (density: ρ_{plume}) and the ambient fluid (density: ρ_a), d is the orifice diameter and V_0 is the exit velocity. We can obtain the critical particle size of r_p at which these two time scales become equal ($St = 1$), by substituting $\alpha = 0.12$ (a typical value for a plume as compiled by *Carazzo et al.* [2006]), $\sigma = 2500$ kg m^{-3}, $d = 10$ m, $V_0 = 20$ m s^{-1}, $\Delta\rho/\rho_a = 0.8$, $\mu = 5 \times$

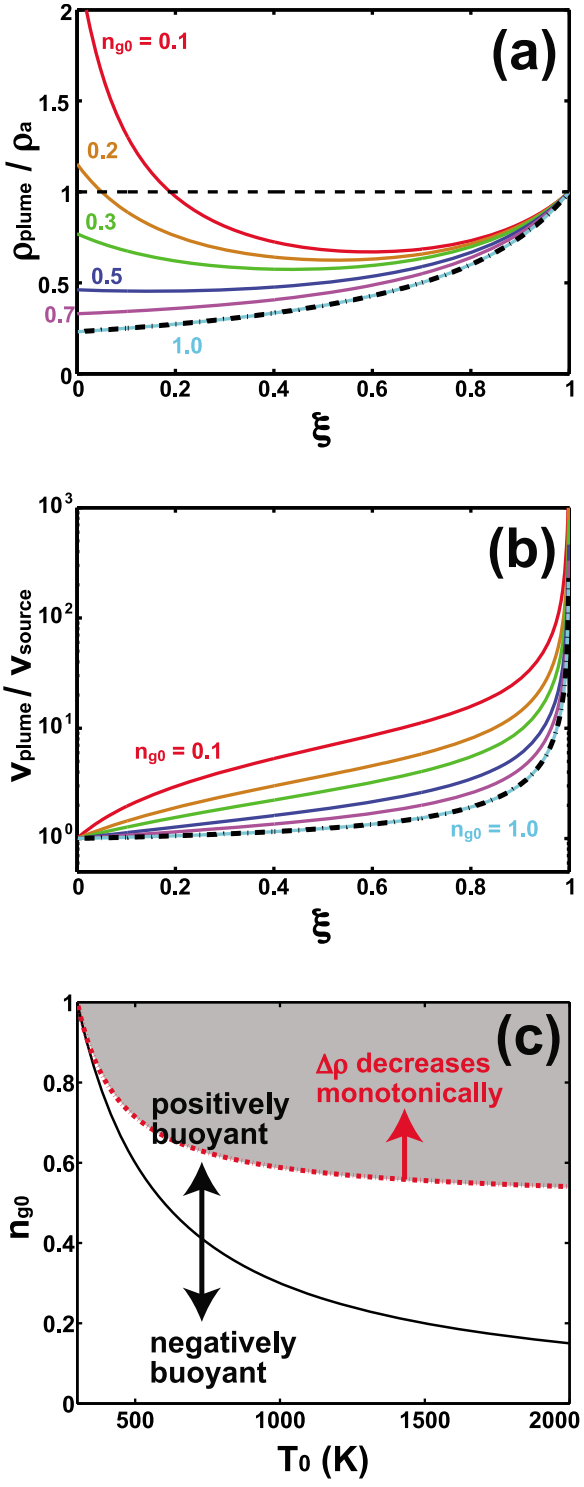

Figure 1. (a) Density of a plume (ρ_{plume}), normalized by the density of air (ρ_a), as a function of mass fraction of the entrained air (ξ). Density was calculated using equation (A7), assuming initial plume temperature $T_0 = 1300$ (K) and ambient air temperature $T_a = 300$ (K), with the mass fraction of volcanic gas in the ejected material (n_{g0}) as the changeable parameter. Cases for $n_{g0} = 0.1$, 0.2, 0.3, 0.5, 0.7, and 1.0 are shown. A black dashed line is the case when a lighter incompressible fluid with a density difference of 7.70×10^2 kg m^{-3} is injected into water, calculated using equation (A13). (b) Same as Figure 1a but for a plume volume (v_{plume}) normalized by the cumulative volume ejected from the source (v_{source}) calculated using equation (A12). Dashed line is that for an incompressible fluid calculated using equation (A14). (c) Density of the volcanic plume in the parameter space of T_0 and n_{g0}. A bold line separates the cases in which the gas is initially positively or negatively buoyant. A dashed red line separates the cases in which there is a density minimum as a function of ξ. When n_{g0} value is larger than critical as shown by the dashed red line, the density difference between the volcanic plume and the ambient air decreases monotonically as entrainment proceeds.

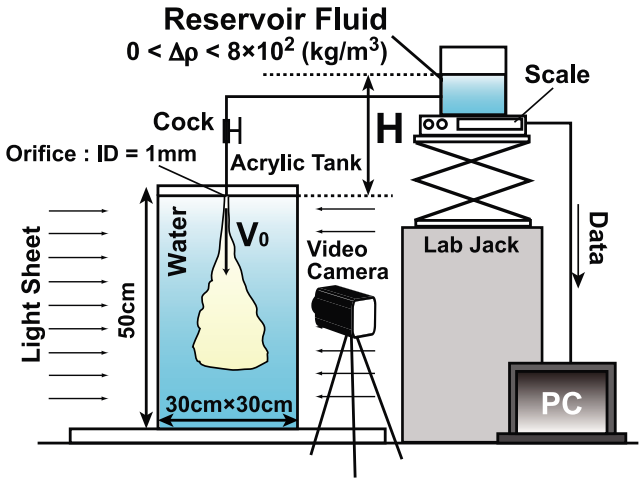

Figure 2. A schematic diagram of the experimental setup.

10^{-5} Pa s, the last 2 values of which correspond to the values for hot volcanic plumes at $T_0 \sim 1300$ K, to obtain

$$r_p \sim 0.13(\mathrm{mm})\left(\frac{z}{100(\mathrm{m})}\right)^{\frac{1}{6}}. \tag{3}$$

Therefore for a typical height scale of the volcanic plume of $z = 100$ m, particles in the size range of $r_p \ll 0.1$ mm, will closely follow the gas flow, since the Stokes number becomes $St \ll 1$.

[16] Second condition is that for particle settling. The condition for particle settling can be approximated by particle settling velocity exceeding the maximum flow velocity, which decreases with height as entrainment proceeds. Particle settling velocity depends on the particle Reynolds number Re_p. Here we assume $Re_p = 2$–2000, which corresponds to the situation in which a volcanic ash of 0.01–10 mm settles at a velocity comparable to the exit velocity $V_0 = 20$ m s^{-1}. At this intermediate particle Reynolds number ($0.4 < Re_p < 500$) the settling velocity becomes [*Bonadonna et al.*, 1998]

$$V_t = 2r_p\left(\frac{4\sigma^2 g^2}{225\mu\rho}\right)^{\frac{1}{3}}, \tag{4}$$

in which ρ is the gas density. Equating equations (2) and (4), we obtain the critical particle radius above which settling occurs,

$$r_p = \frac{1}{2}\cdot\frac{5}{6\alpha}\left(\frac{9\alpha B_0}{10\pi}\cdot\frac{225\mu\rho}{4\sigma^2 g^2}\right)^{\frac{1}{3}} z^{-\frac{1}{3}}. \tag{5}$$

Substituting the same parameter values and $\rho = 1$ kg m^{-3}, we obtain

$$r_p \sim 1(\mathrm{mm})\left(\frac{z}{100(\mathrm{m})}\right)^{-\frac{1}{3}}. \tag{6}$$

Therefore, the particle size with $r_p \ll 1$ mm, will not settle within the typical height of the volcanic plume $z \sim 100$ m.

[17] Combining the above two conditions, for a typical volcanic plume with the scales mentioned above, solid particles can be considered to be homogeneously distributed for $r_p \ll 0.1$ mm. We can make a more detailed estimate by including the temperature dependence of air viscosity and density, but the critical particle size is still of the same order of magnitude.

[18] In our experiments, a dense fluid without solid particles is injected downward, and its density approaches that of the ambient fluid as entrainment proceeds, thus modeling a positively buoyant volcanic plume with a small content of particles with a size of $r_p \ll 0.1$ mm, which is categorized as a "fine ash" by *Bonadonna et al.* [1998]. This situation is similar to those of Strombolian and some vulcanian volcanic plumes as well as steam plumes, fumaroles and hydrothermal plumes without solid particles.

3. Scales and Dimensionless Numbers

[19] There are two important fluxes which drive turbulent plumes. These are the initial specific (i.e., per unit mass) momentum flux $M_0 = \pi(d/2)^2 V_0^2$ and the initial specific buoyancy flux $B_0 = \pi g(\Delta\rho/\rho_a)(d/2)^2 V_0$, in which the variables are explained in section 2. A turbulent plume is initially driven by inertia (jet-like) and later by buoyancy (plume-like). From a dimensional argument, we obtain the characteristic time of the transition from jet-like to plume-like [e.g., *Ai et al.*, 2006] as

$$t_s = \frac{M_0}{B_0} \tag{7}$$

or alternatively the characteristic distance [e.g., *Morton*, 1959; *Fischer et al.*, 1979; *List*, 1982] as

$$L_m = \frac{M_0^{3/4}}{B_0^{1/2}}. \tag{8}$$

The validity of these scales have been verified from velocity measurements [*Papanicolaou and List*, 1988; *Ai et al.*, 2006]. If $t < t_s$ or $z < L_m$, the main driving force of turbulent plumes is inertia, and if $t > t_s$ or $z > L_m$, the main driving force changes to buoyancy. Using these characteristic scales, we can nondimensionalize the time (t) and height of the plume tip (z) which we conduct the experiments. In our experiments, the ranges of t and z are $0 \le t \le 30$ (s) and $0 \le z \le 0.3$ (m), respectively. Accordingly, the nondimensionalized scales become $0 \le t/t_s \le 10^4$ and $0 \le z/L_m \le 10^4$, respectively, thus covering the jet-plume transition.

[20] The effect of the fluid viscosity is characterized by the initial Re,

$$Re = \frac{V_0 d}{\nu}, \tag{9}$$

in which ν is the kinematic viscosity. Viscous diffusion is important in small-scale motions, and its typical time scale becomes

$$t_\nu = \frac{d^2}{\nu}, \tag{10}$$

which we use to nondimensionalize time.

4. Experimental Methods and Parameters

[21] Figure 2 shows a schematic diagram of the experimental setup. We used water and dense aqueous solutions of condensed milk, NaCl and CsCl, colored with a fluorescent

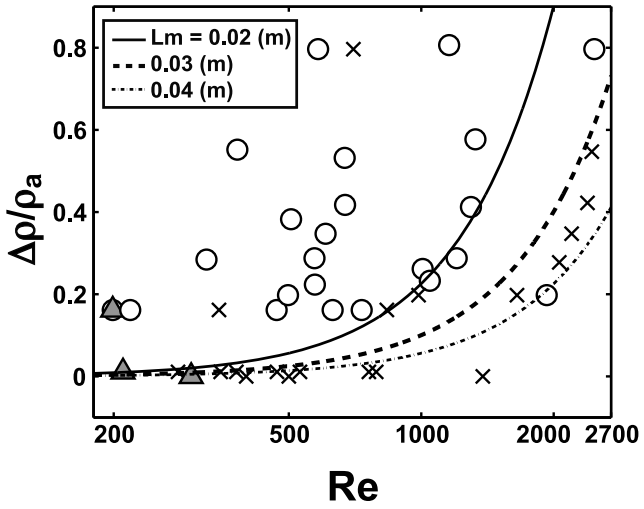

Figure 3. A parameter space of the experiments. Gray triangles, crosses, and circles indicate the cases in which the transitions were observed until regimes II, III, and IV, respectively (see Figure 4 for examples of these regimes). The solid, thick dashed, and thin dashed lines correspond to equation (17) with L_m = 0.02, 0.03, and 0.04 m, respectively.

dye (5×10^{-3} wt %) to generate plumes with a density difference of $0.00 \le \Delta\rho \le 8.00 \times 10^2$ (kg m^{-3}). These fluids are injected downward through an orifice having a circular cross section with an inner diameter of 1 mm. A light sheet is used as an illumination to visualize the cross section of a turbulent plume, and a video camera (1920 × 1080 pixels, 30 fps) is used to record the images of the plume. Exit velocity V_0 was controlled by the height of reservoir fluid above the tank ($0 \le H \le 0.55$ m). V_0 remained constant during the experiment, which was calculated by measuring the decrease of the weight of the reservoir fluid. The list of the experimental runs and their parameters are listed in Table 1. The parameter space of our experiments in terms of *Re* and dimensionless density difference $\Delta\rho/\rho_a$ is summarized in Figure 3. Our experiments are characterized by a large density difference, which is larger than those of previous experiments [*Ai et al.*, 2006] by a factor of ~3, so that we can explore the jet-plume transition and the regime in which the buoyancy becomes important in a laboratory-scale tank.

5. Results

5.1. Shape Evolution Through the Four Regimes

[22] Figure 4 shows an example of the time evolution of a plume for Run 45 (*Re* = 1157 and $\Delta\rho = 8.00 \times 10^2$ kg m^{-3}; auxiliary material).[1] In this experiment, it is jet-like (main driving force is inertia) until t_s = 0.1 s and becomes plume-like (main driving force is buoyancy) after that. From studying the video and its sequential images for a total of 45 experiments, of which Figure 4a is one example, we find that it is possible to define four regimes as a function of elapsed time. Immediately after injection, the plume is laminar whose front has a finger-like shape (regime I, Figure 4b). Next, the vortices with a size of 3 ~ 4 mm appear and form a plume with a head (regime II, Figure 4c). The vortices are advected vertically upward as well as sideways and increase their size as they entrain the ambient fluid. As a consequence the plume gradually transforms into a cone-like shape (regime III, Figure 4d). However this shape does not persist. In particular for the case of $\Delta\rho > 1.62 \times 10^2$ kg m^{-3}, a plume head temporarily inflates above the cone to form a headed cone (regime IV, Figure 4e). Here, regime IV is a temporary deviation from regime III which is only observed for plumes with $\Delta\rho > 1.62 \times 10^2$ kg m^{-3} as classified in Figure 3. The sequence of the shape evolution is shown schematically in Figure 4f.

[23] We also note that for some experiments, the plume meanders as shown in Figure 5. Such meandering appears when $\Delta\rho > 2.00 \times 10^2$ kg m^{-3}, from which we infer that buoyancy is responsible for this phenomenon. This meandering is similar to the flapping behavior reported by *Ai et al.* [2006] which was also observed for a large density difference.

[24] In what follows, we analyzed the binary images to quantitatively determine the onset of the instability and the regimes. Here we use an adaptive image binarization in which we determine the threshold brightness such that the outer edge of the plume of the binary image best coincides with that of the original image.

5.2. Defining the Onset Times of Each Regime

[25] The flow starts with regime I and later transforms into regimes II to IV. We define three time scales τ_{II}, τ_{III}, τ_{IV} to characterize the onsets of the regimes II–IV. In addition we define another time scale τ_{inst} within regime I, which characterizes the onset of instability and the appearance of the vortices.

[26] The flow in regime I is laminar without vortices and therefore indicates that its axial velocity has not decelerated and is equal to the exit velocity V_0. Accordingly, we can calculate the timing of the onset of instability τ_{inst} using the height of the laminar region z_{lam} in the image of a fully developed plume (an arrow in Figure 4e) and V_0 to obtain

$$\tau_{\mathrm{inst}} = \frac{z_{\mathrm{lam}}}{V_0}. \tag{11}$$

In order to confirm the validity of this method to evaluate τ_{inst}, we have made a complimentary experiment using a close-up image taken by a high-speed camera at 500 fps, and measured the actual time taken for the vortices to appear after exiting from the orifice. We compared this time with τ_{inst} calculated using equation (11) from the experiment under the same parameters and find that they agree within 10% error.

[27] When a spherical head develops in regime II, we expect that it becomes apparent as an increase of the height of the centroid h_{C}, which is the 2-D geometrical center of the entire plume area, as shown by stars in Figures 4b–4e. Accordingly, we calculated the dimensionless centroid height $\hat{h}_{\mathrm{C}} = h_{\mathrm{C}}/z$ (inset in Figure 6) as a function of dimensionless time t/t_{v}, and examples are shown in Figure 6. Here z is the flow front height of the plume, t_{v} is the diffusion time (equation (10)). We find that as the plume grows in regime I, $\hat{h}_{\mathrm{C}}$ increases rapidly with time until it approaches a maximum value $\hat{h}_{\mathrm{Cmax}}$ after which it remains approximately constant. By comparing with the images, we find that the plume head

[1] Auxiliary materials are available in the HTML. doi:10.1029/2010JB007633.

Table 1. Experimental Parameters of a Total of 45 Experiments[a]

Run	V_0 (m s^{-1})	μ (mPa s)	$\Delta\rho$ (kg m^{-3})	M_0 (m^4 s^{-2})	B_0 (m^4 s^{-3})	Re	L_m (m)	t_s (s)
1	0.237	1.16	12	4.41×10^{-8}	2.00×10^{-8}	211	2.15×10^{-2}	2.20
2	0.424	1.16	12	1.42×10^{-7}	3.59×10^{-8}	377	8.06×10^{-2}	8.26
3	0.523	1.16	13	2.15×10^{-7}	4.42×10^{-8}	465	3.85×10^{-2}	3.95
4	0.592	1.16	12	2.76×10^{-7}	5.00×10^{-8}	526	4.75×10^{-2}	4.86
5	0.859	1.16	13	5.79×10^{-7}	7.26×10^{-8}	763	5.38×10^{-2}	5.51
6	0.889	1.16	13	6.20×10^{-7}	7.51×10^{-8}	790	7.79×10^{-2}	7.98
7	0.266	1.55	164	5.57×10^{-8}	3.31×10^{-7}	199	6.30×10^{-3}	0.17
8	0.464	1.55	164	1.69×10^{-7}	5.77×10^{-7}	347	1.10×10^{-2}	0.29
9	0.627	1.55	164	3.09×10^{-7}	7.80×10^{-7}	469	1.48×10^{-2}	0.40
10	0.842	1.55	164	5.57×10^{-7}	1.05×10^{-6}	629	1.99×10^{-2}	0.53
11	0.979	1.55	164	7.53×10^{-7}	1.22×10^{-6}	732	2.32×10^{-2}	0.62
12	1.117	1.55	164	9.80×10^{-7}	1.39×10^{-6}	835	2.64×10^{-2}	0.70
13	0.499	1.00	0	1.96×10^{-7}	0	500	-	-
14	1.377	1.00	0	1.49×10^{-6}	0	1380	-	-
15	0.316	1.16	14	7.84×10^{-8}	2.67×10^{-8}	280	2.87×10^{-2}	2.94
16	0.394	1.16	14	1.22×10^{-7}	3.34×10^{-8}	350	3.58×10^{-2}	3.67
17	0.267	1.55	160	5.57×10^{-8}	3.31×10^{-7}	199	6.30×10^{-3}	0.17
18	0.293	1.55	160	6.70×10^{-8}	3.63×10^{-7}	218	6.91×10^{-3}	0.18
19	0.299	1.00	0	7.04×10^{-8}	0	300	-	-
20	0.399	1.00	0	1.25×10^{-7}	0	400	-	-
21	0.233	0.922	287	4.27×10^{-8}	5.10×10^{-7}	325	4.16×10^{-3}	0.08
22	0.339	0.929	385	9.04×10^{-8}	9.98×10^{-7}	506	5.22×10^{-3}	0.09
23	0.238	0.969	555	4.45×10^{-8}	1.01×10^{-6}	382	3.05×10^{-3}	0.04
24	0.367	1.13	800	1.06×10^{-7}	2.25×10^{-6}	583	3.91×10^{-3}	0.05
25	0.736	0.924	264	4.25×10^{-7}	1.48×10^{-6}	1007	1.37×10^{-2}	0.29
26	0.785	0.927	235	4.85×10^{-7}	1.41×10^{-6}	1046	1.55×10^{-2}	0.34
27	0.767	0.933	200	4.62×10^{-7}	1.17×10^{-6}	986	1.64×10^{-2}	0.40
28	1.523	0.967	550	1.82×10^{-6}	6.41×10^{-6}	2441	1.96×10^{-2}	0.28
29	1.500	0.933	200	1.77×10^{-6}	2.28×10^{-6}	1928	3.21×10^{-2}	0.77
30	0.388	0.933	200	1.18×10^{-7}	5.89×10^{-7}	498	8.29×10^{-3}	0.20
31	0.434	0.928	226	1.48×10^{-7}	7.47×10^{-7}	573	8.73×10^{-3}	0.20
32	0.409	0.922	290	1.32×10^{-7}	9.05×10^{-7}	572	7.26×10^{-3}	0.15
33	0.415	0.924	350	1.35×10^{-7}	1.11×10^{-6}	606	6.69×10^{-3}	0.12
34	0.442	0.934	420	1.53×10^{-7}	1.42×10^{-6}	671	6.50×10^{-3}	0.11
35	0.420	0.962	535	1.38×10^{-7}	1.72×10^{-6}	670	5.47×10^{-3}	0.08
36	0.441	1.13	800	1.52×10^{-7}	2.70×10^{-6}	701	4.69×10^{-3}	0.06
37	1.556	1.13	800	1.90×10^{-6}	9.54×10^{-6}	2473	1.66×10^{-2}	0.20
38	1.257	0.933	225	1.29×10^{-6}	1.95×10^{-6}	1650	2.75×10^{-2}	0.66
39	1.484	0.923	280	1.73×10^{-6}	3.17×10^{-6}	2059	2.68×10^{-2}	0.55
40	1.504	0.924	350	1.78×10^{-6}	4.02×10^{-6}	2196	2.43×10^{-2}	0.44
41	1.565	0.935	425	1.92×10^{-6}	5.08×10^{-6}	2386	2.29×10^{-2}	0.38
42	0.863	0.922	290	5.82×10^{-7}	1.90×10^{-6}	1204	1.53×10^{-2}	0.31
43	0.854	0.933	415	5.74×10^{-7}	2.71×10^{-6}	1297	1.26×10^{-2}	0.21
44	0.822	0.979	580	5.32×10^{-7}	3.65×10^{-6}	1328	1.03×10^{-2}	0.15
45	0.731	1.13	800	4.18×10^{-7}	4.53×10^{-6}	1157	7.74×10^{-3}	0.09

[a] V_0, exit velocity; μ, viscosity; $\Delta\rho$, density difference; M_0, initial specific momentum flux; B_0, initial specific buoyancy flux; Re, Reynolds number; L_m (equation (8)) and t_s (equation (7)), characteristic length and time scales, respectively, of jet-plume transition.

becomes evident just before $\hat{h}_C$ becomes a maximum ($\hat{h}_{Cmax}$). Accordingly we define the onset time of regime II, τ_{II} as the time at which the centroid height becomes $h_C = 0.85\hat{h}_{Cmax}$ as indicated by stars in Figure 6.

[28] Regime III is characterized by a cone-like shape, and when viewed from the side, it can be approximated as a triangle. We therefore calculated the deviation from the triangle in terms of a misfit (%)

$$\text{misfit}(\%) = \frac{|S_P - S_T|}{S_P}, \tag{12}$$

where S_P and $S_T = h_w W/2$ are the measured areas of the plume excluding the laminar region, and the fitted triangle (height h_w, width W), as shown in the inset of Figure 7. When calculating the misfit in equation (12), we use the area below the height h_w at which the plume width W becomes the widest.

[29] Examples of the evolution of the misfits are shown in Figure 7, from which we find that the misfits are initially large (>50%) but decrease with time to a value of about 10%. Comparing with the images, we find that most of the plumes transform into regime III at misfit ≤15%. Accordingly, we define the onset of regime III as the time when the misfit first becomes ≤15% which are indicated by stars in Figure 7.

[30] In Figure 7, we also show a case in which the misfit increased again by an amount of ≥20% after the transition to regime III. This is a consequence of the temporary inflation of the plume head (regime IV) as shown schematically in Figure 7 (inset). For this particular experiment, there were a total of three such transitions as indicated by arrows, which we also confirmed from the images. Accordingly we define the onset of regime IV when the misfit increased by an amount of ≥20% after attaining a minimum. We classified the experiments according to the cases in which the transi-

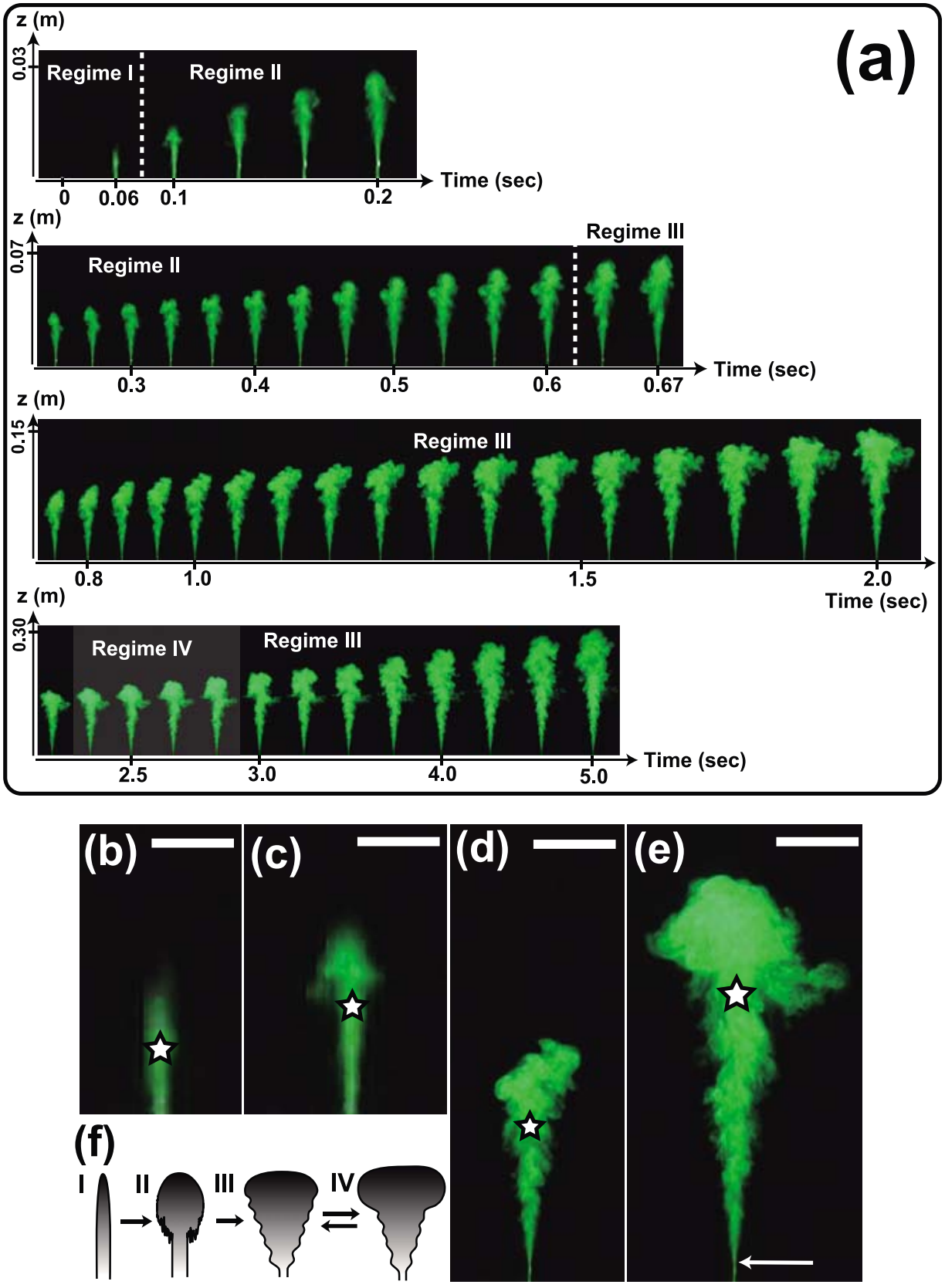
(a)
z (m)
0.03
Regime I
Regime II
0
0.06
0.1
0.2
Time (sec)
z (m)
0.07
Regime II
Regime III
0.3
0.4
0.5
0.6
0.67
Time (sec)
z (m)
0.15
Regime III
0.8
1.0
1.5
2.0
Time (sec)
z (m)
0.30
Regime IV
Regime III
2.5
3.0
4.0
5.0
Time (sec)
(b)
(c)
(d)
(e)
(f)
I
II
III
IV

Figure 4

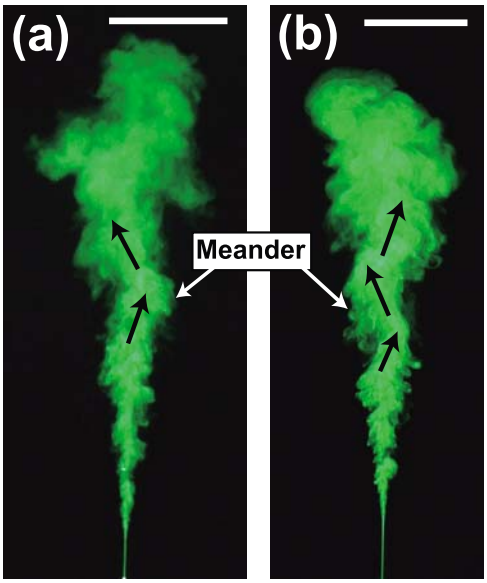

Figure 5. Examples of meandering flow at (a) t = 5 s for Run 24 (Re = 583, $\Delta\rho = 8.00 \times 10^2$ kg m^{-3}) and (b) t = 7.5 s for Run 31 (Re = 573, $\Delta\rho = 2.26 \times 10^2$ kg m^{-3}). Such meandering motion is observed when $\Delta\rho \geq 2.26 \times 10^2$ kg m^{-3}. Scale bars are 50 mm.

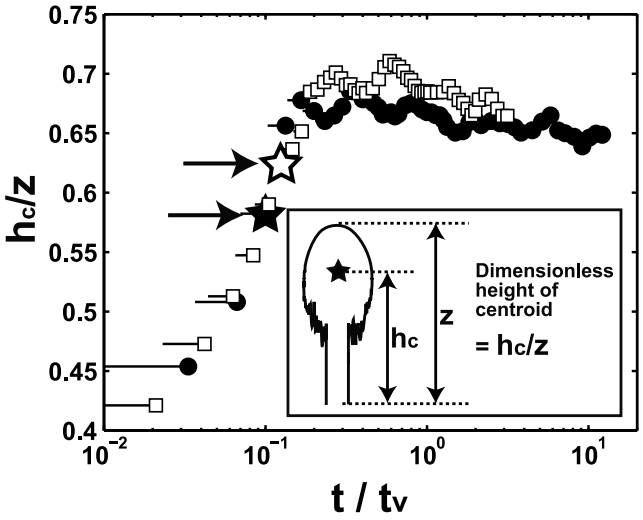

Figure 6. Examples of the evolution of the height of the centroid (see inset), which are used to define the onset of regime II. Here the time is normalized by the diffusion time (equation (10)). The data shown are for Run 14 (Re = 1380, $\Delta\rho = 0.00$ kg m^{-3}, solid circles) and Run 24 (Re = 583, $\Delta\rho = 8.00 \times 10^2$ kg m^{-3}, open squares). Solid and open stars indicate the determined onset time of regime II.

tions were observed until regime II, III, or IV, which we plot in Figure 3. Figure 3 shows that the transition to regime IV preferentially occurs for small Re or large $\Delta\rho/\rho_a$, i.e., when the buoyancy is large compared to inertia.

[31] Although regime IV is a temporary deviation from regime III, we consider that it should be distinguished from regime III. Plumes are generally considered to eventually develop into a self-similar cone-like shape, but our experiments show that this is a simplified image. We consider that such deviation from self-similarity is characteristic of plumes after the jet-plume transition, which is achieved in many of our experiments because we injected fluids with large density. Indeed, the appearance of large-scale vortices after the plumes become cone-like has been noted previously [*Ai et al.*, 2006]. We also note that jets and plumes in regime III appear very similar, and that regime IV is one feature that is characteristic of plumes.

5.3. Parameter Dependence of the Onset Times

[32] Figure 8a shows a summary of the three onset times τ_{inst}, τ_{II} and τ_{III} for a total of 45 experiments plotted as a function of Re. Vertical axis is time normalized by the diffusion time t_v (equation (10)). Figure 8a shows that the onset times have negative power law dependences on Re (i.e., larger Re results in earlier onsets). In order to find the buoyancy dependence of the power law exponents of the onset time–Re relation, we made two fittings separated at a threshold density of $\Delta\rho_C = 2.25 \times 10^2$ kg m^{-3}. Here, $\Delta\rho_C$ was chosen such as to maximize the difference of the power law exponents for the onsets of regime III. From the fits we find that for $\Delta\rho \leq \Delta\rho_C$ (hereafter, small $\Delta\rho$ case, plotted as filled markers), the power law exponents for all transitions are $\simeq -2$. On the other hand, for $\Delta\rho > \Delta\rho_C$ (hereafter, large $\Delta\rho$ case, plotted as open markers) the power law exponents become $\simeq -1$, whose absolute values are smaller than those of the small $\Delta\rho$ case (see caption for the details of the fits). In particular, the power law exponent for the onset of regime III is smaller by a factor of 2. This large difference of power law exponent arises from the data at $Re < 800$, in which the onset of regime III becomes earlier for large $\Delta\rho$ case (i.e., under the same Re, a plume with a larger buoyancy transits to regime III earlier). From the fits we can also compare the timing of the onset of instability τ_{inst}, with the time needed to develop into a fully developed flow (τ_{III}). From the fits using small $\Delta\rho$ case, we obtain $\tau_{III} \sim 25\tau_{inst}$.

[33] In Figure 8b, we plot the same result using the conventionally used height scale (z/d) instead of time, from which we find that the correlation becomes poorer (see caption), It is

Figure 4. Time evolution of a plume for Run 45 (with initial Re = 1157 and a density difference of $\Delta\rho = 8.00 \times 10^2$ kg m^{-3}). (a) Time-lapse images of the evolution, (b) a finger regime (I) at t = 0.06 s, (c) a plume with head regime (II) at t = 0.10 s, (d) a cone-like regime (III) at t = 1.07 s, and (e) a headed-cone regime (IV) at t = 2.67 s. A scale bar is 10 mm for Figures 4b and 4c and 50 mm for Figures 4d and 4e. Stars indicate the location of the centroid of the total plume area, and an arrow in Figure 4e indicates the height of the laminar region (z_{lam}). We define time zero when the injected fluid first appears from the orifice, and accordingly the maximum time error is −0.03 s due to the frame rate of the video. (f) A schematic diagram showing the sequential transitions of the four regimes. For some parameters, evolutions only until regime II or III are observed (see Figure 3).

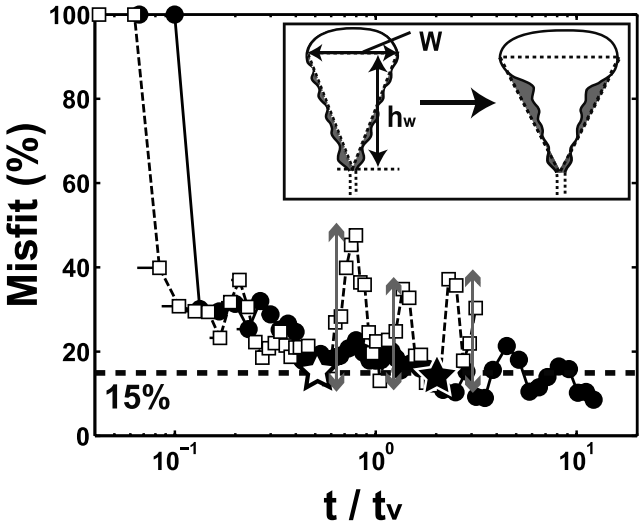

Figure 7. Examples of the evolution of the misfits (deviation from a triangular shape), which are used to define the onset of regime III. The data shown are for Run 14 (Re = 1380, $\Delta\rho$ = 0.00 kg m^{-3}, solid circles) and Run 24 (Re = 583, $\Delta\rho = 8.00 \times 10^2$ kg m^{-3}, open squares). Solid and open stars indicate the determined onset time of regime III. The three arrows indicate the temporary transitions from regime III to regime IV. The gray zones shown schematically in the inset are the regions of the misfit from the triangle.

possible that the regime transition height is relatively insensitive to buoyancy because there are two compensating effects when buoyancy is large; a faster onset time and smaller deceleration.

Table 2. Spreading Rates, Half Angle, and Entrainment Constants for Jets (4 Runs) and Plumes (41 Runs)

	Minimum	Maximum	Mean	Standard Deviation
Jet ($\Delta\rho$ = 0 kg m^{-3})				
Spreading rate (W_h/h_{tw})	0.16	0.24	0.21	0.05
Half angle (deg)	8.88	13.74	11.88	2.63
Entrainment constant	0.07	0.11	0.09	0.02
Plume ($\Delta\rho \geq$ 12 kg m^{-3})				
Spreading rate (W_h/h_{tw})	0.14	0.26	0.19	0.03
Half angle (deg)	7.89	14.76	10.96	1.73
Entrainment constant	0.12	0.18	0.16	0.04

5.4. Spreading Rates and Entrainment Constants

[34] From the images, we can measure the spreading rates (or equivalently the half angles) of the plumes and calculate the entrainment constants α using the analytical models for jet ($\Delta\rho$ = 0) and plume ($\Delta\rho \neq 0$), whose results are summarized in Table 2. Following the method used by *Patrick* [2007a], we measured the maximum half width of the visible edge of the plume (W_h) and the height of the maximum width (h_{tw}), and linearly fitted the data to obtain the spreading rate, W_h/h_{tw}, which is then used to calculate the half angle (deg) = arctan(W_h/h_{tw}) · (180/π). α can then be calculated from the analytical models [e.g., *Morton et al.*, 1956; *Turner*, 1969; *Patrick*, 2007a] as

$$\alpha = \frac{1}{2} \cdot \frac{b}{h_{tw}} \quad \text{(for jet)}, \tag{13}$$

$$\alpha = \frac{5}{6} \cdot \frac{b}{h_{tw}} \quad \text{(for plume)}. \tag{14}$$

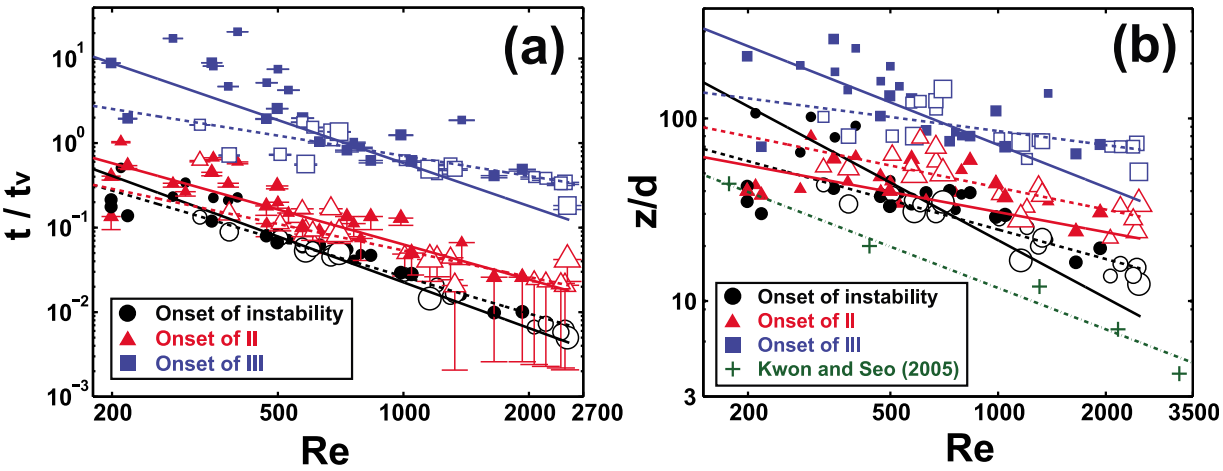

Figure 8. (a) The three onset times as functions of Re for a total of 45 experiments. Circles (black), triangles (red), and squares (blue) correspond to τ_{inst}, τ_{II}, and τ_{III}. Marker sizes correspond to the magnitude of the density difference $\Delta\rho$, and solid and open markers represent the cases for $\Delta\rho \leq \Delta\rho_C$ and $\Delta\rho > \Delta\rho_C$, respectively, with $\Delta\rho_C = 2.25 \times 10^2$ kg m^{-3}. Solid and dotted lines are power law fits of the respective cases for each onset. The power law exponents for small (large) $\Delta\rho$ cases for the onset of instability, regime II, and regime III are -1.8 ± 0.2 (-1.5 ± 0.1), -1.4 ± 0.2 (-1.0 ± 0.4), and -1.7 ± 0.4 (-0.8 ± 0.3), respectively. The correlation coefficient of the fit for regime III is 0.90 (0.83) for the respective $\Delta\rho$ ranges. (b) Same as Figure 8a but in terms of distance nondimensionalized by the orifice diameter. The power law exponents for small (large) $\Delta\rho$ cases for regime III are -0.79 ± 0.3 (-0.25 ± 0.2), with correlation coefficients of 0.80 (0.65). Pluses indicate the height at which the instability starts measured from the photographs of experiments at $\Delta\rho$ = 0 kg m^{-3} by *Kwon and Seo* [2005].

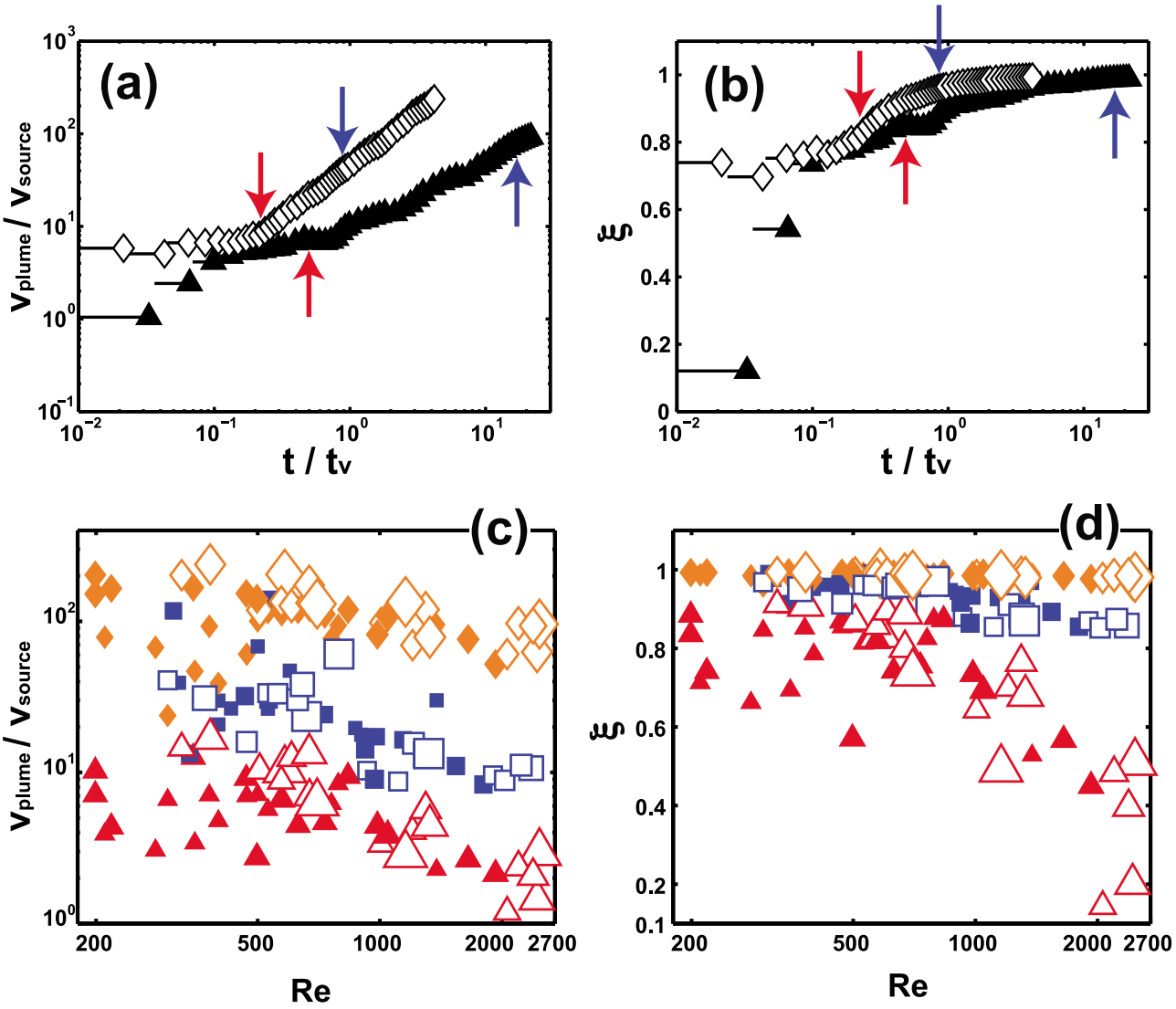

Figure 9. (a) Examples of the time evolution of the plume volume nondimensionalized by the cumulative volume of the injected fluid for similar *Re*. Volume was calculated using equation (15). The data shown are for Run 2 (Re = 377, $\Delta\rho = 1.20 \times 10^1$ kg m^{-3}, filled triangles) and Run 23 (Re = 382, $\Delta\rho = 5.55 \times 10^2$ kg m^{-3}, open diamonds). Red and blue arrows indicate the onsets of regimes II and III. (b) Same as Figure 9a but for the time evolution of mass fraction of entrained fluid (ξ). (c) Dimensionless plume volume at the onsets of regimes II (red triangles) and III (blue squares), at maximum height (orange diamonds) plotted as a function of *Re*. Solid and open markers are the same as in Figure 8. (d) Here ξ as a function of *Re* calculated from the volume using equation (A14).

Here b is the characteristic half width of a plume at which entrainment occurs [*Turner*, 1962], and can be expressed as $b = 0.9W_h$ for starting plumes which is the case in our experiments [*Patrick*, 2007a]. We find that spreading rates (half angles) of the jets and plumes are 0.21 ± 0.05 (11.88° ± 2.63°) and 0.19 ± 0.03 (10.96° ± 1.73°), respectively, indicating that the values are the same within errors. For entrainment constants (α) we obtained $\alpha = 0.09 \pm 0.02$ for jets and 0.16 ± 0.04 for plumes.

[35] Here we may compare the values obtained above with those of previous works. Using the same method, *Turner* [1962] obtained the spreading rate (half angle) of plumes as 0.18 ± 0.03 (10.2° ± 1.72°), which is close to our result. Jets and plumes having similar velocity spreading rates have also been shown by *Wang and Law* [2002]. Similarly, the entrainment constants obtained agree within 30% error, with those of previous works in which α was obtained using velocity measurements [e.g., *Fischer et al.*, 1979; *Papanicolaou and List*, 1988; *Wang and Law*, 2002; *Kaminski et al.*, 2005].

5.5. Volume Increase With Entrainment

[36] We can also calculate the volume of the plume (v_{plume}) using the images excluding the laminar region assuming

$$v_{\text{plume}} = \pi \int_0^{h_M} \left(\frac{W(z)}{2}\right)^2 dz, \qquad (15)$$

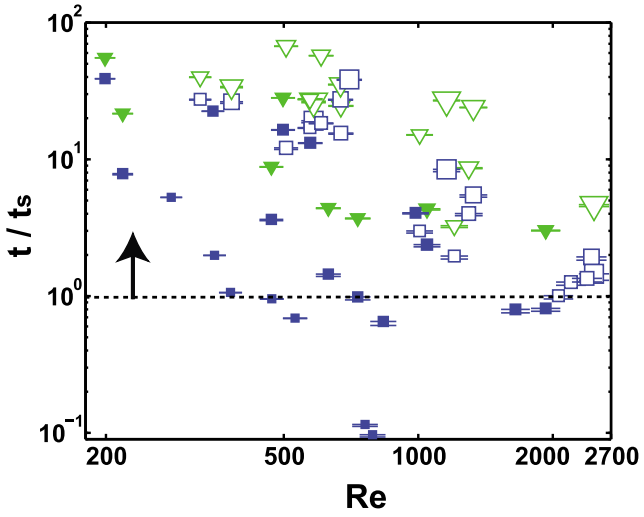

Figure 10. Onset times of regime III and regime IV normalized by t_s (equation (7)) as a function of *Re*. Blue squares and green triangles indicate the onset of regimes III and IV, respectively. Solid and open markers correspond to small and large $\Delta\rho$ cases (same as in Figure 8). The dotted line is $t/t_s = 1$.

where h_M is the height of the plume tip and $W(z)$ is the plume width at each height.

[37] In Figure 9a, we show two examples of the time evolution of the plume volume. Here similar to Figure 1b, the volume is nondimensionalized by the cumulative volume (v_{source}) injected at the source until the respective times. In Figure 9a, two cases at $Re \sim 380$ with different $\Delta\rho$ are shown. Comparing the two cases, we find that the volume increase is faster for a large $\Delta\rho$ case. In Figure 9a, we have also indicated the timing of the onsets of regime II and III. Figure 9a shows that the timing of the onset of regime II for the two cases is the same within a factor of 3 (red arrows), whereas for regime III, the large $\Delta\rho$ case becomes earlier by an order of magnitude (blue arrows) as we have shown already in Figure 8a. In Figure 9b, we plot the corresponding time evolution of the mass fraction of the entrained fluid (ξ) which were calculated from the plume volume using equation (A14). The plot shows that the increase of ξ is faster for larger $\Delta\rho$, indicating a larger volume of entrained fluid per unit time.

[38] In Figure 9c, we plot the volumes of the plumes at the onsets of regime II and III, and the maximum value (i.e., at the height when the plume tip leaves the field of view) in the experiments. The plot shows that the dimensionless volume of the plumes at the onsets of regime II and III decrease with *Re*. Similarly in Figure 9d, we plot ξ at the regime onsets. The plot shows that at the onset of regime II, the mass fraction of the entrained fluid (ξ) is $\xi > 0.1$, indicating that apart from the accumulation of the injected fluid, entrainment is responsible for the formation of a plume head. At the onset of regime III, the entrained mass fraction becomes $\xi > 0.7$, indicating that most of the fluid within the plume is that of the entrained fluid. We also remark that for $Re < 800$, the volume and entrained fluid at the onset of regime II is larger for a large $\Delta\rho$ case, as indicated by open markers. This is the consequence of a larger volume of entrained fluid per unit time until the onset of regime II, as shown in Figures 9a and 9b.

6. Discussion

6.1. Interpretation of the Regimes

[39] First we consider the onset time of the instability τ_{inst}, in which the buoyancy plays a negligible role in our parameter range. We assume that this instability arises from the shear at the viscous boundary layer adjacent to the plume with a thickness of $\delta \sim \sqrt{\nu t}$ that grows with time. We can define a local *Re* as $Re_l = V_0\delta/\nu$ and consider that instability occurs when it exceeds the critical value, i.e., $Re_l > Re_c$. This relation can be rewritten using the initial *Re* (equation (9)) and t_v (equation (10)) as

$$\frac{t}{t_v} > \left(\frac{Re}{Re_c}\right)^{-2}, \tag{16}$$

which explains the power law exponent for τ_{inst} being close to −2 in Figure 8a. By fitting equation (16) to the data for τ_{inst}, we obtain $Re_c = 100 \pm 47$. We also note that when the buoyancy is small, the power law exponents of the onset times of regimes II and III are also ~ −2, indicating that the successive growth time of the instability also scales in proportion to equation (16).

[40] Next we consider the reason for the earlier onset of regime III for highly buoyant plumes at $Re < 800$; that is, onset is earlier for plumes with large $\Delta\rho$ than those with small $\Delta\rho$. Buoyant plumes are less decelerated than jets, and sustains a large shear at the plume edge and this causes the earlier transition and the modification of the power law exponent. In Figure 10, we compare the onset time of regime III (τ_{III}) with that of jet-plume transition t_s (equation (7)), which is the time scale in which the buoyancy overwhelms inertia. The plot shows that for all cases in which the onset of regime III became earlier (i.e., open square markers at $Re < 800$), the condition $\tau_{III}/t_s > 10$ is satisfied, indicating that for these cases buoyancy indeed exceed inertia at the onset of regime III. A condition needed for the earlier transition can be diagnosed further by analyzing the onset times of regime II (τ_{II}). We find that for the cases in which the onset to regime III became earlier, the condition $\tau_{II}/t_s > 1$ is satisfied, indicating that buoyancy already exceeded inertia at the onset time of regime II as well. On the other hand, for all cases in $Re > 800$, the onset time is $\tau_{II}/t_s < 1$, indicating that inertia was still larger than buoyancy. This suggests that $\tau_{II}/t_s > 1$ at the onset of regime II is necessary for the earlier transition to regime III.

[41] Here, we emphasize that in our experiments, onset of regime III is unrelated to the jet-plume transition. This transition is observed for a jet ($\Delta\rho = 0$), for which case it is unrelated to the jet-plume transition. For plumes ($\Delta\rho \neq 0$), we can compare the timing of the onset of regime III (τ_{III}) with the jet-plume transition time t_s (Figure 10). The plot shows that τ_{III} do not scale well with t_s, and that for most experiments, $\tau_{III}/t_s > 1$, indicating that onset of regime III occurs after the jet-plume transition. Alternatively, we can compare the heights of the onset of regime III (z_{III}) with that of jet-plume transition (L_m) and similarly find that z_{III} do not scale well with L_m and that for all experiments, $z_{III}/L_m > 1$.

[42] Another effect of buoyancy is the transition to regime IV, which we observed for nonzero $\Delta\rho$ cases only (Figure 3). In Figure 10, we also plot the onset times of regime IV (τ_{IV}), from which we find that for all cases in which regime IV appeared (triangle markers) $\tau_{IV}/t_s > 3$, indicating that buoyancy exceeding inertia is also required for the appearance of regime IV. This implies that we need to monitor for a sufficiently long time to observe regime IV. In other words, if the same experiments were done using a larger tank, we may be able to observe regime IV even for the parameters which we did not observe in our experiments. To evaluate this quantitatively, in Figure 3 we draw curves given by

$$\frac{\Delta\rho}{\rho_a} = \left(\frac{9.5\times10^{-6}}{L_m(\mathrm{m})}\right)^2 Re^2, \tag{17}$$

which is identical to equation (8) expressed using the experimental values. Here L_m is the changeable parameter and we draw three curves with different values of L_m. We find that a curve with $L_m = 0.03$ (m) reasonably separates the cases in which regime IV was observed or not (Figure 3). Since, we track the plume up to a height of 0.3 m, this suggests that we need to monitor to a height of at least $z \sim 10L_m$ to observe regime IV.

[43] We next consider the result in which the dimensionless volume v_{plume}/v_{source} at the onsets of regimes II and III, decrease with *Re* (Figure 9c). Here we find that both v_{plume} and v_{source} decrease with *Re*, but the former decreases more rapidly with *Re*. At the onset of regime II, $v_{source} = V_0\tau_{II}$, and v_{source} is only weakly dependent on *Re* because of the compensating change of V_0 and τ_{II} as *Re* increases. Concerning the onset of regime II, the plot shows that at $Re < 800$, v_{plume} is larger for a large $\Delta\rho$ case. This seems to arise from plume head being more inflated at the onset of regime II for the large $\Delta\rho$ case. Similarly, for the onset of regime III, we find that v_{plume} decreases with *Re*. However for regime III, no clear relation between v_{plume} and $\Delta\rho$, as well as that between v_{source} and *Re* were found.

[44] Here we comment on the possible effect of the nozzle shape on regime onsets. It is known that jets from noncircular nozzles are more unstable and have a larger entrainment constants compared to circular jets [*Gutmark and Grinstein*, 1999]. This suggests that the regime transition time is likely to become earlier for the noncircular jets. Accordingly, if the same experiments were conducted using a noncircular nozzle, the scaling relationship is likely to be modified such that the onset times will become earlier (i.e., smaller prefactor of the scaling relationship). In addition, noncircular jets are not axisymmetric, and the spreading rate become anisotropic, which implies that the shape may appear different compared to circular jets.

[45] Finally, we compare the regime transitions obtained from our work with previous works. In Figure 8b we plot the height scale in which the instability starts using the photographs in the work by *Kwon and Seo* [2005], who conducted similar experiments at comparable *Re* but for jets. Comparison shows that the height scale agree within a factor of 2, and that it also decreases with *Re*. The earlier transition to developed flow for buoyant plumes is also consistent with the compiled analyses based upon the velocity measurements [*Carazzo et al.*, 2006].

6.2. Implications for Volcanic Plumes

[46] We consider applying our results to hot volcanic plumes with a small content of fine ash such as Strombolian eruptions as we discussed in section 2. Comparing the images of the volcanic plumes with those of our experiments, we find that similar shapes do exist. For example, a high-velocity jet in Figure 3a of *Patrick* [2007a] and those described as "starting plume" are similar to the shapes at regime I and at the transition from regime I to regime II, respectively, in our experiments. This similarity suggests that the newly devised method to characterize plume shape may also be applied in actual volcanic plumes to define the regimes. Many volcanic plumes analyzed by *Patrick* [2007a] do not seem to evolve until the cone-like shape (regime III) forms, possibly because the eruption duration is not long enough. However, a well-collimated (small *d*), high-velocity (large V_0) plume [*Patrick et al.*, 2007, Figure 4e] is observed to transform into a cone-like shape (regime III). The scaling relation for the transition height (z) of regime III (Figure 8b), when expressed in dimensional form, becomes $z \propto d^{0.21}V^{-0.79}$ and $z \propto d^{0.75}V^{-0.25}$ for small and large density differences, respectively, (see caption), which are consistent with the smaller transition heights for such plumes. In addition, a helical motion similar to meandering in our experiments (Figure 5) has also been reported at Stromboli [e.g., *Patrick*, 2007a, Figure 9b] and is also evident in ash-steam plumes rising at Mount St. Helens [*Rosi et al.*, 2003].

[47] *Patrick* [2007a] described that a starting plume eventually transforms into a "rooted thermal" characterized by a bulbous head whose shape is apparently similar to that of regime IV. We can compare the ratio, (plume front radius)/(steady plume radius), as used by *Patrick* [2007a]. For the plumes in regime IV of our experiments, this ratio becomes 1.7 ± 0.3, which is indeed close to the values in the range of 1.5–2, reported for rooted thermals in the work by *Patrick* [2007a]. However there are also differences. First, when we compare the maximum and mean spreading rates, we obtained the values of 0.26 and 0.19 ± 0.03 (see Table 2), whereas they obtained the values of 0.41 and 0.24 ± 0.02, respectively, for volcanic plumes [*Patrick*, 2007a]. This indicates that the "headed cone" has a smaller spreading rate compared to a rooted thermal. In addition, we note that the headed cone (regime IV) is a temporary deviation from regime III whereas such temporary excursion into rooted thermal is not documented by *Patrick* [2007a]. Furthermore, the plume beneath the rooted thermal has a columnar shape [e.g., *Patrick*, 2007a, Figure 3c] whereas that beneath the headed cone has a "cone-like" shape. It seems that the time-dependent source flux is responsible for the formation of rooted thermal.

[48] Here we evaluate the characteristic scales and dimensionless numbers of the volcanic plumes. For a typical Strombolian volcanic plume with $d = 10$ m, $V_0 = 20$ m s^{-1} with a temperature of 1300 K, the same values as those used in estimates in sections 2 and 3, the characteristic time and length scales of the jet-plume transition at which the driving force changes from inertia to buoyancy become $t_s \simeq 2$ s and $L_m \simeq 21$ m, respectively. Therefore, similar to our experiments, a jet-plume transition can be recorded in videos. We note however, that Reynolds number of a volcanic plume is orders of magnitude larger than those of our experiments. For

the same volcanic plume, using the molecular kinematic viscosity of air $\nu \sim 10^{-5}$ m^2 s^{-1}, the initial *Re* becomes $Re \sim 2 \times 10^7$, which is 4 orders of magnitude larger than the *Re* in our experiments, and hence the viscous effects are relatively more important in the experiments. It is known that a fully developed turbulence occurs at $Re > 10^4$ [e.g., *Dimotakis*, 2005] and therefore we cannot simply extrapolate our experiments to higher *Re*. Despite these differences, we consider that several implications can be given based upon our experiments.

[49] First, we discuss the magnitude of buoyancy relative to inertia. Here, we emphasize that although our experiments do not cover the *Re* of volcanic plumes, it covers the jet-plume transition. Under a constant source flux, our experiments indicate that the only shape which is characteristic of large buoyancy is the regime IV, and that the sequence of shape changes until they become fully developed (regimes I–III) is similar. Rather, our experiments suggest that the timing of the regime change, may be a better measure of buoyancy as evident from Figure 8a. One application of the scaling law obtained from Figure 8a is to use the ratio of the two onset times; $t^* = \tau_{III}/\tau_{inst}$. In our experiments, for $\Delta\rho \leq 2.25 \times 10^2$ kg m^{-3}, this ratio becomes $t^* = 36.0Re^{0.02}$ and is nearly independent of *Re*, whereas for $\Delta\rho \geq 2.60 \times 10^2$ kg m^{-3}, it becomes $t^* = 0.20Re^{0.72}$ and increases with *Re*. If the source temperature of the plume at the vent (i.e., the buoyancy) is approximately constant, this suggests that t^* may be used as a proxy for constraining the temperature of the volcanic plumes by measuring the exit velocity (*Re*) at the same vent. As a first step, we propose that measurements of t^* be made for volcanic plumes rising from the same vent to see whether any scaling law exists between V_0 and t^*. Similarly, we can also define the ratio which compares the onsets of regime II and instability, $t^{**} = \tau_{II}/\tau_{inst}$, which may be used for the case in which regime III does not appear. The method described above can be used in conjunction with the thermal imaging, which gives the plume temperature after it has entrained a certain fraction of ambient air. The scaling law obtained from our experiments are intended to constrain the source temperature and can therefore compliment thermal imaging.

[50] Second we discuss the large-scale structure of the volcanic plume, which is similar to those of our experiments, despite the orders of magnitude difference in Reynolds number. For example although the finger-like region of a volcanic plume consists of many small vortices, and therefore is different from laminar flow in our experiments, the overall columnar structure is similar. In volcanic plumes, because of the high Reynolds number, it is likely that such small-scale eddies are already present in the vent, prior to eruption. The presence of eddies within the mean pipe flow in the conduit will transport the axial momentum from the center to the rim of the vent, thereby giving rise to the eddy viscosity and reducing the effective Reynolds number. This may be the cause for the apparent similarity with regime I in our experiments. Relevance of eddy viscosity as the origin of large-scale structure of volcanic plumes has been discussed already [*Chakraborty et al.*, 2006], and there are many examples of large-scale vortices or wakes in the atmosphere (e.g., Karman vortex streets) and ocean. For example, *Van Dyke* [1982, Figures 172–173] shows that oceanic wake behind a tanker at $Re \sim 10^7$ is very similar to a laboratory wake at $Re = 4300$. Another example is given in the work of *Samimy et al.* [2003, p. 78], in which a vortex generated by an impacting water drop at $Re \sim 10^2$ is very similar to the large-scale vortex of an atomic bomb explosion ($Re \geq 10^9$). Here they propose that the similarity arises due to a similar initial geometry of the vorticity generation. The basic configuration of the flow of our experiments and that of the volcanic plume are the same, and the vortices are generated by the shear instability caused by the inertia and buoyancy. We speculate that the similarity of the large-scale structure in volcanic plumes may also be such an example. Plumes at Reynolds number comparable to that of a volcanic plume ($Re \simeq 2 \times 10^8$) was reported by *Mungal and Holingsworth* [1989], which also showed the presence of a large-scale flow. These suggest that the large-scale flow will be similar for experiments and in volcanic plumes. It would be interesting to examine the shape change in the near-field region in such flows to see how the timing of the regime onsets scale with exit velocity and density difference.

7. Conclusions

[51] We conducted a series of laboratory experiments in which dense fluids are injected downward, which are simplified model of a positively buoyant volcanic plume with a small content of fine ($r_p \ll 0.1$ mm) ash, such as a Strombolian ash plume. We studied how the plume shape evolves with time, and how the exit velocity (*Re*) and density difference ($\Delta\rho$) control its evolution. From image analyses we find that it is possible to define four regimes as a function of elapsed time. Initially, the plume has a "finger-like" shape (regime I). As the plume decelerates and entrains the ambient fluid, it forms a "plume head" (regime II), which later transforms into a "cone-like" self-similar shape (regime III). In regime III, jets and plumes appear similar, which is manifested by a similar value of the spreading rates (half angles). However, when $\Delta\rho$ is above a critical value, the plume head temporarily inflates above the cone to form a "headed cone" (regime IV). We devised new methods to define the onset times using the height of the laminar region (for the onset of instability), height of the centroid of the entire plume area (for regime II) and the deviation from the triangle (for regime III and IV). We find that for a small density difference, the onset times of the instability and the regimes scales as Re^{-2}, which can be understood from the growth of viscous shear instability. However, for a large density difference, the transition of regime III becomes earlier and the power law exponent becomes ~ -1, one feature which can be used to constrain density difference.

[52] We compared the images of the volcanic plumes with those of our experiments. We find that the large-scale structures of the volcanic plumes are similar to the plume shapes observed in our experiments, although the *Re* of the volcanic plumes is 4 orders of magnitude larger than those of our experiments.

[53] We consider that the similarity of the flow configuration and the effect of eddy viscosity may be the apparent cause of the similarity. From the experiments we infer that similar scaling relation between the regime onset times and the exit velocity may exist in the volcanic plumes. We

suggest that by using the same method to characterize plume shape, and by studying the timing, rather than heights, of the regime onsets, we may be able to constrain the source temperature of the volcanic plumes.

Appendix A: Density and Volume Change Associated With Entrainment

[54] The density and volume of a mixture of the ejected material and air changes with entrainment. Here we summarize their expressions following *Woods* [1988] and *Suzuki et al.* [2005].

[55] A volcanic plume is a mixture of volcanic gas, solid particles and entrained air. We can define the initial mass fraction of volcanic gas n_{g0} in the ejected material as

$$n_{g0} = \frac{n_{\mathrm{Gas}}}{n_{\mathrm{Gas}} + n_{\mathrm{Solid}}} \tag{A1}$$

and the mass fraction of the entrained air (or fluid) ξ as

$$\xi = \frac{n_{\mathrm{Air}}}{n_{\mathrm{Gas}} + n_{\mathrm{Solid}} + n_{\mathrm{Air}}}, \tag{A2}$$

where n_{Gas}, n_{Solid}, n_{Air} are the mass fractions of volcanic gas, solid particles and entrained air, respectively, which add up as $n_{\mathrm{Gas}} + n_{\mathrm{Solid}} + n_{\mathrm{Air}} = 1$. The temperature of a mixture of ejected material and air T_m can be expressed as

$$T_m = \frac{(1-\xi)C_{p0}T_0 + \xi C_{pa}T_a}{(1-\xi)C_{p0} + \xi C_{pa}}, \tag{A3}$$

where T_0, T_a are the temperatures, C_{p0}, C_{pa} are the specific heats with subscripts 0 and a indicating that of ejected material (solid + volcanic gas) and air, respectively. The plume density ρ_{plume} can be expressed as

$$\frac{1}{\rho_{\mathrm{plume}}} = \frac{n_{\mathrm{Solid}}}{\sigma} + \frac{\left(n_{\mathrm{Gas}}R_g + n_{\mathrm{Air}}R_a\right)T_m}{p}, \tag{A4}$$

where σ is the solid particle density, p is the pressure inside a plume assuming that it is equal to atmospheric pressure, R_g and R_a are the gas constants of volcanic gas and air, respectively. For a pressure-balanced plume we take $p = \rho_a R_a T_a$, and we assume $R_a = R_g$, $C_{p0} = C_{pa}$ for simplicity because these are of the same order of magnitude, from which we obtain T_m and ρ_{plume} as

$$T_m = (1-\xi)T_0 + \xi T_a, \tag{A5}$$

$$\frac{1}{\rho_{\mathrm{plume}}} = \frac{n_{\mathrm{Solid}}}{\sigma} + \frac{(n_{\mathrm{Gas}} + n_{\mathrm{Air}})T_m}{\rho_a T_a}. \tag{A6}$$

For a volcanic plume with $T_0 = 1300$ K, $T_a = 300$ K and $\sigma = 2500$ kg m^{-3}, the volume occupied by solid particles (first term on the RHS of equation (A6)) is <0.1 that of the volcanic gas and entrained air (second term) whenever $n_{g0} > 10^{-3}$. Accordingly, for volcanic plumes, we may neglect the first term and we use this approximation in what follows.

[56] We can rewrite equation (A1) as $n_{g0} = n_{\mathrm{Gas}}/(1-\xi)$, and using this we obtain $n_{\mathrm{Gas}} + n_{\mathrm{Air}} = (1-\xi)n_{g0} + \xi$. Substituting this relation and equation (A5) into equation (A6), the density of a volcanic plume relative to air becomes

$$\frac{\rho_{\mathrm{plume}}}{\rho_a} = \left[\left\{(1-\xi)n_{g0} + \xi\right\} \cdot \frac{(1-\xi)T_0 + \xi T_a}{T_a}\right]^{-1}, \tag{A7}$$

which we use to draw the curves in Figure 1a.

[57] Next, the volume of a volcanic plume v_{plume} is

$$v_{\mathrm{plume}} = \frac{M_{\mathrm{Gas}} + M_{\mathrm{Solid}} + M_{\mathrm{Air}}}{\rho_{\mathrm{plume}}}, \tag{A8}$$

where M indicates the mass of each components. From equation (A2), $M_{\mathrm{Air}} = \xi(M_{\mathrm{Gas}} + M_{\mathrm{Solid}} + M_{\mathrm{Air}})$, and we can rewrite equation (A8) as

$$v_{\mathrm{plume}} = \frac{M_{\mathrm{Gas}} + M_{\mathrm{Solid}}}{\rho_{\mathrm{plume}}(1-\xi)}. \tag{A9}$$

We define the density and the cumulative volume of the ejected material prior to entrainment as ρ_{source} and v_{source}, respectively. Here v_{source} is expressed as $v_{\mathrm{source}} = (M_{\mathrm{Gas}} + M_{\mathrm{Solid}})/\rho_{\mathrm{source}}$ which we use to nondimensionalize v_{plume} to obtain

$$\frac{v_{\mathrm{plume}}}{v_{\mathrm{source}}} = \frac{\rho_{\mathrm{source}}}{\rho_{\mathrm{plume}}(1-\xi)}. \tag{A10}$$

The density of the source fluid ρ_{source} is expressed as

$$\frac{1}{\rho_{\mathrm{source}}} = \frac{1-n_{g0}}{\sigma} + \frac{n_{g0}}{\rho_g}, \tag{A11}$$

where ρ_g is the density of the volcanic gas. We can rewrite equation (A10) using equation (A11) and the equations of state for air and volcanic gas ($\rho_a = p/R_aT_a$ and $\rho_g = p/R_aT_0$), and similarly neglect the first term of the right hand side in equation (A11) to obtain

$$\frac{v_{\mathrm{plume}}}{v_{\mathrm{source}}} = \frac{(1-\xi)n_{g0} + \xi}{(1-\xi)n_{g0}} \cdot \frac{(1-\xi)T_0 + \xi T_a}{T_0}, \tag{A12}$$

which we use to draw the curves in Figure 1b.

[58] We can similarly derive the density and volume change for the case of experiments which become

$$\frac{\rho_{\mathrm{plume}}}{\rho_a} = \frac{\rho_g}{(1-\xi)\rho_a + \xi\rho_g} \tag{A13}$$

and

$$\frac{v_{\mathrm{plume}}}{v_{\mathrm{source}}} = \frac{\rho_g}{\rho_a} \cdot \frac{\xi}{(1-\xi)} + 1. \tag{A14}$$

Note that equations (A7) and (A12) reduce to equations (A13) and (A14), respectively, when $n_{g0} = 1$ and using equation of state $\rho_a \propto 1/T_a$ and $\rho_g \propto 1/T_0$.

[59] Next, we derive the condition needed for the volcanic plumes to become positively buoyant at the vent exit, which is $\rho_{\mathrm{plume}_0} < \rho_a$, where ρ_{plume_0} is the plume density at the exit. Using equation (A4) this condition becomes

$$\frac{1}{\rho_{\mathrm{a}}} < \frac{1-n_{g0}}{\sigma} + \frac{n_{g0}R_gT_0}{\rho_a R_a T_a}. \tag{A15}$$

Similar to equation (A6), we can neglect the first term on the right hand side of equation (A15) and assuming $R_a = R_g$, we obtain

$$n_{g0} \geq \frac{T_a}{T_0}, \tag{A16}$$

which we use to draw the solid black line in Figure 1c.

[60] Finally, we consider the condition for the density increasing monotonically with entrainment. Differentiating equation (A7), we can find ξ which minimizes the density as

$$\xi_m = \frac{1}{2}\left(\frac{T_0}{T_0 - T_a} - \frac{n_{g0}}{1 - n_{g0}}\right). \tag{A17}$$

ξ_m decreases with n_{g0} (Figure 1a) and therefore the condition for a monotonic density change becomes $\xi_m \leq 0$, which reduces to

$$n_{g0} \geq \frac{T_0}{2T_0 - T_a}, \tag{A18}$$

which we use to draw the red dashed line in Figure 1c.

[61] We can classify three styles in which the density changes with ξ, as functions of T_0 and n_{g0} which we show in Figure 1c: (1) heavier than the ambient air at the vent exit, (2) lighter than ambient air at the exit and there is a plume density minimum as a function of ξ, and (3) lighter than the ambient air at the exit and the plume density monotonically approach that of the ambient air.

[62] **Acknowledgments.** We thank M. Patrick and an anonymous reviewer for carefully reading the manuscript and A. Namiki for discussions. This work was supported by KAKENHI (18204038, 18740272).

References

Ai, J., A. Law, and S. Yu (2006), On Boussinesq and non-Boussinesq starting forced plumes, *J. Fluid Mech.*, *558*, 357–386.

Bonadonna, C., G. G. J. Ernst, and R. S. J. Sparks (1998), Thickness variations and volume estimates of tephra fall deposits: The importance of particle Reynolds number, *J. Volanol. Geotherm. Res.*, *81*, 173–187.

Carazzo, G., E. Kaminski, and S. Tait (2006), The route to self-similarity in turbulent jets and plumes, *J. Fluid Mech.*, *547*, 137–148.

Carazzo, G., E. Kaminski, and S. Tait (2008), On the rise of turbulent plumes: Quantitative effects of variable entrainment for submarine hydrothermal vents, terrestrial and extra terrestrial explosive volcanism, *J. Geophys. Res.*, *113*, B09201, doi:10.1029/2007JB005458.

Chakraborty, P., G. Gioia, and S. Kieffer (2006), Volcán Reventador's unusual umbrella, *Geophys. Res. Lett.*, *33*, L05313, doi:10.1029/2005GL024915.

Chouet, B., N. Hamisevicz, and T. R. McGetchin (1974), Photoballistics of volcanic jet activity at Stromboli, Italy, *J. Geophys. Res.*, *79*, 4961–4976.

Clarke, A. B., J. C. Phillips, and K. N. Chojnicki (2009), An investigation of Vulcanian eruption dynamics using laboratory analogue experiments and scaling analysis, in *Studies in Volcanology*, vol. 2, edited by T. Thordarson et al., pp. 155–166, Geol. Soc. of London, London.

Dimotakis, P. E. (2005), Turbulent mixing, *Annu. Rev. Fluid Mech.*, *37*, 329–356.

Dimotakis, P. E., R. C. Miake-Lye, and D. A. Papantoniou (1983), Structure and dynamics of round turbulent jets, *Phys. Fluids*, *26*, 3185–3192.

Fischer, H. B., E. J. List, R. C. Y. Koh, J. Imberger, and N. H. Brooks (1979), Turbulent jets and plumes, in *Mixing in Inland and Coastal Waters*, pp. 315–389, Academic, San Diego, Calif.

Formenti, Y., T. H. Druitt, and K. Kelfoun (2003), Characterization of the 1997 Vulcanian explosions of Soufriére hills volcano, Montserrat, by video analysis, *Bull. Volcanol.*, *65*, 587–605.

Gutmark, E. J., and F. F. Grinstein (1999), Flow control with noncircular jets, *Annu. Rev. Fluid Mech.*, *31*, 239–272.

Kaminski, E., S. Tait, and G. Carazzo (2005), Turbulent entrainment in jets with arbitrary buoyancy, *J. Fluid Mech.*, *526*, 361–376.

Kaye, N. B., and G. R. Hunt (2009), An experimental study of large area source turbulent plumes, *Int. J. Heat Fluid Flow*, *30*, 1099–1105.

Kieffer, S. W., and B. Sturtevant (1984), Laboratory studies of volcanic jets, *J. Geophys. Res.*, *89*, 8253–8268.

Kwon, S. J., and I. W. Seo (2005), Reynolds number effects on the behavior of non-buoyant round jet, *Exp. Fluids*, *38*, 801–812.

List, E. J. (1982), Turbulent jets and plumes, *Annu. Rev. Fluid Mech.*, *14*, 189–212.

Mori, T., and M. Burton (2009), Quantification of the gas mass emitted during single explosions on Stromboli with the SO_2 imaging camera, *J. Volcanol. Geotherm. Res.*, *188*, 395–400.

Morton, B. R. (1959), Forced plumes, *J. Fluid Mech.*, *5*, 151–163.

Morton, B. R., G. I. Taylor, and J. S. Turner (1956), Gravitational turbulent convection from instantaneous and maintained sources, *Proc. R. Soc. London, Ser. A*, *234*, 1–23.

Mungal, M. G., and D. K. Holingsworth (1989), Organized motion in a very high Reynolds number jet, *Phys. Fluids A*, *1*(10), 1615–1623.

Ogden, D. E., K. H. Wohletz, G. A. Glatzmaier, and E. E. Brodsky (2008a), Numerical simulations of volcanic jets: Importance of vent overpressure, *J. Geophys. Res.*, *113*, B02204, doi:10.1029/2007JB005133.

Ogden, D. E., G. A. Glatzmaier, and K. H. Wohletz (2008b), Effects of vent overpressure on buoyant eruption columns: Implications for plume stability, *Earth Planet. Sci. Lett.*, *268*, 283–292.

Papanicolaou, P. N., and E. J. List (1988), Investigations of round vertical turbulent buoyant jets, *J. Fluid Mech.*, *195*, 341–391.

Papanicolaou, P. N., I. G. Papakonstantis, and G. C. Christodourou (2008), On the entrainment coefficient in negatively buoyant jets, *J. Fluid Mech.*, *614*, 447–470.

Parfitt, E. A., and L. Wilson (2008), *Fundamentals of Physical Volcanology*, 230 pp., Blackwell, Oxford, U. K.

Patrick, M. R. (2007a), Dynamics of Strombolian ash plumes from thermal video: Motion, morphology, and air entrainment, *J. Geophys. Res.*, *112*, B06202, doi:10.1029/2006JB004387.

Patrick, M. R. (2007b), The gas content and buoyancy of Strombolian ash plume, *J. Volcanol. Geotherm. Res.*, *166*, 1–6, doi:10.1016/j.jvolgeores.2007.06.001.

Patrick, M. R., A. J. L. Harris, M. Ripepe, J. Dehn, D. A. Rothery, and S. Calvari (2007), Strombolian explosive styles and source conditions: Insights from thermal (FLIR) video, *Bull. Volcanol.*, *69*, 769–784.

Rosi, M., P. Papale, L. Lupi, and M. Stoppato (2003), *Volcanoes*, 335 pp., Firefly Books, Tonawanda, N. Y.

Sahatapy-Engel, S. T., and A. J. L. Harris (2009), Thermal-image-derived dynamics of vertical ash plumes at Santiaguito volcano, Guatemala, *Bull. Volcanol.*, *71*, 827–830.

Samimy, M., K. S. Breuer, L. G. Leal, and P. H. Steen (2003), *A Gallery of Fluid Motion*, 118 pp., Cambridge Univ. Press, Cambridge, U. K.

Solovitz, S. A., and L. G. Mastin (2009), Experimental study of near-field air entrainment by subsonic volcanic jets, *J. Geophys. Res.*, *114*, B10203, doi:10.1029/2009JB006298.

Sparks, R. S. J. (1986), The dimensions and dynamics of volcanic eruption columns, *Bull. Volcanol.*, *48*, 3–15.

Suzuki, Y. J., and T. Koyaguchi (2009), A three-dimensional numerical simulation of spreading umbrella clouds, *J. Geophys. Res.*, *114*, B03209, doi:10.1029/2007JB005369.

Suzuki, Y. J., and T. Koyaguchi (2010), Numerical determination of the efficiency of entrainment in volcanic eruption columns, *Geophys. Res. Lett.*, *37*, L05302, doi:10.1029/2009GL042159.

Suzuki, Y. J., T. Koyaguchi, M. Ogawa, and I. Hachisu (2005), A numerical study of turbulent mixing in eruption clouds using a three-dimensional fluid dynamics model, *J. Geophys. Res.*, *110*, B08201, doi:10.1029/2004JB003460.

Turner, J. S. (1962), The "starting plume" in neutral surrounding, *J. Fluid Mech.*, *13*, 356–369.

Turner, J. S. (1969), Buoyant plume and thermals, *Annu. Rev. Fluid Mech.*, *1*, 22–29.

Van Dyke, M. (1982), *An Album of Fluid Motion*, 176 pp., Parabolic Press, Stanford, Calif.

Wang, H., and A. W. Law (2002), Second-order integral model for a turbulent buoyant jet, *J. Fluid Mech.*, *459*, 397–428.

Woods, A. W. (1988), The fluid dynamics and thermodynamics of eruption columns, *Bull. Volcanol.*, *50*, 169–193.

Woods, A. W., and C.-C. P. Caulfield (1992), A laboratory study of explosive volcanic eruptions, *J. Geophys. Res.*, *97*, 6699–6712.

Yamamoto, H., I. M. Watson, J. C. Phillips, and G. J. Bluth (2008), Rise dynamics and relative ash distribution in Vulcanian eruption plumes at Santiaguito Volcano, Guatemala, revealed using an ultraviolet imaging camera, *Geophys. Res. Lett.*, *35*, L08314, doi:10.1029/2007GL032008.

Yokoo, A. (2009), Continuous thermal monitoring of the 2008 eruptions at Showa crater of Sakurajima volcano, Japan, *Earth Planets Space*, *61*, 1345–1350.

S. Kitamura and I. Sumita, Graduate School of Natural Science and Technology, Kanazawa University, Kanazawa 920-1192, Japan. (kitamura@hakusan.s.kanazawa-u.ac.jp)